https://doi.org/10.1016/j.apenergy.2021.116825

An ultra-low-frequency, broadband and multi-stable tri-hybrid energy harvester for enabling the next-generation sustainable power

Chen Wang[a], Siu-Kai Lai[a,b,*], Jia-Mei Wang[a], Jing-Jing Feng[c], Yi-Qing Ni[a,b]

[a] *Department of Civil and Environmental Engineering, The Hong Kong Polytechnic University, Kowloon, Hong Kong, P.R. China*

[b] *Hong Kong Branch of National Rail Transit Electrification and Automation Engineering Technology Research Center, The Hong Kong Polytechnic University, Kowloon, Hong Kong, P.R. China*

[c] *Tianjin Key Laboratory for Advanced Electromechanical System Design and Intelligent Control, School of Mechanical Engineering, Tianjin University of Technology, Tianjin, P.R. China*

Abstract

This work presents a highly miniaturized, ultra-low-frequency, broadband, multi-stable, frequency up-converted and tri-hybrid portable energy harvester to harness structural and biomechanical vibration energy efficiently. This energy harvester is developed by using a novel multi-stability-based frequency up-converted approach, in which two new configurations of magneto-multi-stable oscillators are closely integrated. Hence, the displacement stroke of low-frequency vibration and the mechanical energy transfer process can almost completely overlap, and consequently magnify the power output and power density under low-frequency broadband vibration sources. By hybridizing two impact-driven piezoelectric generators, an array-type electromagnetic generator, a sliding-mode triboelectric nanogenerator and a contact-separation triboelectric nanogenerator in a highly compact arrangement, more electric power can be generated from a single mechanical motion, which can successfully enhance the output performance. A fabricated prototype of the present design is tested using both shaker excitations and body-induced motions. Under the mechanical shaker test, the prototype works well at a wide bandwidth of 1−11 Hz under 1 g (= 9.8 m s^{-2}) and generates a maximum output power of 85.65 mW across the optimum resistance loads, corresponding to the normalized power density of 3.69 mW cm^{-3} g^{-2} at 3 Hz under 1 g. During the human activity tests (i.e., walking, slow running, and handshaking), the prototype also shows good performance under different wearable positions of the human body and can power up 20 thermohygrometers and 296 commercial light-emitting diodes continuously. The present energy harvester is a promising application to enable as a sustainable power source for wearable/portable electronics and wireless monitoring systems.

*Corresponding author. *E-mail address*: sk.lai@polyu.edu.hk

Keywords: Tri-/quad-stable nonlinearity, Piezoelectric-electromagnetic-triboelectric harvester, Frequency up-conversion, Structural vibration, Biomechanical energy

1. Introduction

The myriad of possibilities afforded by the Internet of Things (IoT), which create an ecosystem in which things in the physical world can be electronically monitored and controlled, has inspired a surge of innovation. Evolving the IoT and artificial intelligence in smart cities leads to the tremendous development of wireless sensor networks (WSN), the demand for mobile or distributed power supplies is thus of paramount importance. Hitherto, the majority of electronics are powered by conventional electrochemical batteries, which are limited in lifespan and required periodic charging and replacement. Abandoned batteries can also cause environmental hazards. To address these technical demands, harvesting energy from vibration-induced sources has been the subject of studies to develop built-in energy harvesters for various potential applications, thereby achieving a self-sustained system without external power sources [1]. Advancing self-powered energy-harvesting techniques is an encouraging "green" solution that may facilitate the development of IoT-based wireless technologies for remote monitoring, safety prognosis and information exchange in various engineering sectors. In reality, vibration sources are ubiquitous in our ambient environment, which can be converted into electricity to power IoT sensors [2, 3]. Generally, there are three main mechanisms that have been extensively exploited to convert mechanical vibration into electrical energy, namely piezoelectric [4], electromagnetic [5] and triboelectric [6] approaches. Each mechanism has their unique features and limitations. For example, electromagnetic harvesters can perform better in terms of current output, while piezoelectric and triboelectric harvesters can generate higher voltage levels [7]. This forms a good complementary in the power generation process of energy harvesting.

Ambient vibration sources (e.g., structural vibration and human motions) are generally low-frequency, random and time-varying. Particularly, various motions of the human body, e.g., handshaking, walking, running, and jumping, also possess the characteristics of large-amplitude, low-frequency and fluctuation over time [8]. Since this vibration energy is distributed over a wide spectrum of frequencies, it is necessary for resonant-based harvesters to explore some resonant-frequency-matching strategies, such as frequency tuning mechanisms [9], multi-degree-of-freedom structures [10] or nonlinear dynamical systems [11], to broaden the operation bandwidths. However, frequency tuning mechanisms are not efficient under random or rapidly changing frequency inputs, they usually require a complex design or external power that can reduce the energy harvesting efficiency [12]. While the design of multi-degree-of-freedom systems can broaden the operation bandwidth at the cost of bigger size in dimensions, leading to the reduction of power density of such harvesters. In contrast, the application of multi-stable nonlinearity-enhanced mechanisms in energy harvesting technology plays a crucial role in improving the working performance of vibration-based energy harvesters under low excitation levels. Consequently, nonlinear energy harvesters, possessing mono-stable [13], bi-stable [5], tri-stable [14], quad-stable [15] and even quin-stable [16] characteristics, have been intensively investigated to broaden the operation bandwidth. It is evident that more stable equilibrium states (e.g., the septuple-stable nonlinearity-enhanced mechanical frequency up-conversion mechanism firstly

proposed by the authors) are beneficial for large-amplitude oscillations and lower threshold excitations under certain conditions [17]. Recently, a multi-degree-of-freedom tri-stable harvester array was proposed to effectively combine the advantages of both multi-degree-of-freedom and nonlinear approaches [18]. It is worth noting that although tri-stable and higher-order multi-stable characteristics have shown great potential in low-frequency and broadband vibration energy harvesting techniques [19], there are few studies on accommodating such characteristics in portable-type energy harvesters. Consider the time-varying nature of human-induced motions, a well-designed high-order multi-stable mechanical system with advanced energy conversion mechanisms is required to improve the harvesting efficiency of portable energy harvesters.

Another technical challenge for harvesting sufficient energy from low-frequency human motions lies in the fact that the generated power of a resonant generator is proportional to the cube of the vibration frequency and is too low to be utilized when under a low-frequency excitation [20]. Besides, matching the resonant frequency of a harvester with low-frequency excitations requires a low stiffness and/or a heavy inertial mass, leading to a large displacement stroke and thus resulting in more occupied space. To address this dilemma, numerous frequency up-conversion (FUC) approaches have been proposed to bridge the gap between low-frequency excitations and high-frequency responses of such transducer units. Generally, FUC approaches can be implemented through five avenues: mechanical impact [19], mechanical plucking [21], pulsed magnetic force [22], pulsed acceleration [23], and internal resonance [24]. These implementations allow the transducer units to operate at high frequencies via an external mechanical energy transferred using a non-resonant or low-frequency oscillator. However, a relatively large displacement stroke is still essential to ensure that the use of low-frequency oscillators can harness sufficient energy from an ambient low-frequency vibration source. This reduces the compactness and power density of these energy harvesters inevitably. To address this issue, our group proposed a quin-stability enhanced FUC approach, which allows the displacement stroke of the low-frequency vibration process to partially overlap with that of the mechanical energy transfer process via inter-well motions [15, 16]. The partially overlapping method can improve the intensity and duration of the mechanical energy transfer process and reduce the total displacement stroke, and consequently realize wideband energy harvesting from low-intensity and low-frequency vibration sources. Making use of this mechanism, it can boost the power density almost 31.7 times than that of a conventional FUC counterpart [16]. However, this FUC approach is adversely affected by gravitational fields and suffers a low harvesting efficiency under a low-intensity vertical vibration source [17]. Hence, a more compact design based on the FUC approach is required to be further developed for wearable and portable applications.

By integrating multiple energy-harvesting mechanisms, more electric power can be harvested from a single mechanical movement, which could not only meet the power demand of numerous wearable and portable electronics, but also can take the advantages of different mechanisms into a

single package [25]. There are several studies on the design of hybrid harvesters, in which the electromagnetic mechanism is often coupled with the piezoelectric ortriboelectric mechanisms to fabricate different kinds of "2-in-1" hybrid harvesters [7, 8, 26–31]. To further improve the harvesting efficiency at low frequencies, several "3-in-1" design approaches were also reported to accommodate more energy-harvesting mechanisms into a single hub [17, 32–34]. Although these works are very interesting and innovative, due to their power density and dynamic performance at low frequencies, sustainably powering commercial wearable electronics or IoT systems by harvesting low-intensity human-induced vibrations remains a grand challenge. Coupling low-frequency human-induced vibrations into a "3-in-1" hybrid harvester requires an advanced and ingenious design scheme.

In this work, a highly miniaturized, ultra-low-frequency, broadband, multi-stable, frequency up-converted and tri-hybrid portable energy harvester is proposed to sustainably power wearable/portable electronics. This harvester is developed using a novel multi-stability based FUC approach, which is implemented by the highly compact combination of two new configurations of magneto-multi-stable oscillators. Benefiting from the new FUC approach, the harvester can exhibit a quad-stable state in its horizontal direction, this makes the displacement stroke of the low-frequency vibration and the mechanical energy transfer process overlap almost completely. Hence, it can improve the power output and power density under low-frequency, low-intensity, and wideband vibration sources. When operating vertically, the mechanical system of this harvester can degrade into a tri-stable system with a wide band and high efficiency similar to the horizontal state. Moreover, by hybridizing two impact-driven piezoelectric generators, an array-based electromagnetic generator, a sliding-type triboelectric nanogenerator and a contact-separation triboelectric nanogenerator in a highly compact arrangement, more power can be generated from a single mechanical motion, further improving the power density. Through the theoretical and experimental studies, the mechanical properties and electrical performance of the portable energy harvester are investigated for a low-frequency range covering general human-induced motions. In addition, experimental demonstrations of the proposed harvester are carried out for charging storage units, brightening light-emitting diodes (LEDs), and powering thermohygrometers. With a wider bandwidth and higher power density than similar devices reported recently, the present design makes a significant step toward clear energy harvesting from ultra-low-frequency vibration sources in many engineering fields.

2. System design and working mechanism

2.1. Configuration of the multi-stable oscillators

As a power source of portable and wearable electronic devices, portable energy harvesters should possess a high electrical damping property and a compact-size design. However, many configurations of tri-stable energy harvesters are confined by employing a cantilever beam structure and/or multiple external fixed magnets, this is not conducive to achieve a compact design that can maximize the electrical damping under mechanical motions. More seriously, although human-induced motions have

a higher intensity in the vertical direction, these tri-stable configurations failed to consider the effect of gravity in their design processes. When working along the direction of gravitational fields, the potential function of these tri-stable configurations will deform asymmetrically and even degrade into mono-stable states with an asymmetric deep potential well, thereby confining the frequency responses into narrow-band and small oscillation amplitudes.

To address the above issues, two new multi-stable configurations, namely Type I and Type II, are firstly proposed in this work. In Fig. 1(a), the configuration Type I consists of a fixed magnet A with a width of d_1 and a parallel moving-magnet B poled reversely with a width of d_2 ($d_2 > d_1$). The initial distance between the center of two magnets is h. Several spacers A and B are attached on the moving-magnet as a proof mass, where the spacer A has the same dimensions with that of the magnet B. Under the force of gravity, the proof mass will compress the lower linear spring with an initial deformation of d_g, which is equal to the gap distance between the free end of the upper linear spring and the upper spacer A. For comparison, the configuration Type II has two magnets B poled in the same direction with the magnet A and it is separated by two spacers B and one spacer A, as shown in Fig. 1(e). Under a vertical base excitation, the slider will oscillate and make impact between the upper and lower springs to achieve a frequency-up conversion process. By varying the parameters d_2 and h, both configurations can conduct the dynamic behaviour of mono-stable, bi-stable or tri-stable states, as shown in Figs. 1(b) and 1(f), respectively. In the case of d_2 = 6.35 mm (1/4 in), with the increase of h, the potential function of the configuration Type I can pass through a tri-stable state to a bi-stable state, and further to a mono-stable state, as shown in Fig. 1(c). For the configuration Type II, the transition path to a mono-stable state is directly come from a tri-stable state, as shown in Fig. 1(g). In both transition stages mentioned above, the increase of h can reduce the potential barrier(s) so that the inter-well oscillation can occur more easily, but it also decreases the distance between two outermost stable equilibrium positions significantly, resulting in the reduction of inter-well motion amplitudes. Therefore, the value of h should be properly chosen by taking the characteristics of ambient vibration sources into consideration.

Since human-induced motions are usually at low frequencies [35, 36], a high-magnification FUC approach coupling with a magnet array configuration is introduced to bridge the gap between the characteristics of the energy transducers and human-induced motions. A similar distribution of the multi-stable parameter regions between Types I and II makes it possible to directly constitute a combined configuration with optimized dynamic characteristics. Fig. 1(i) shows the combined configuration in a vertical direction, which can be considered as a direct combination of two Type I and two Type II configurations with shared fixing-magnets. Due to the combination, the alternating polarity magnet arrays can form a phase shift of the magnetic flux density during sliding up and down to increase the efficiency of the electromagnetic transducer. The stiffness of the linear spring increases to $4k$ to further strengthen the magnification of FUC. In the case of d_2 = 6.35 mm, the potential energy function of the combined configuration can transform from a tri-stable state to a bi-stable state, and

then return back to a tri-stable state, and finally reach to a mono-stable state, as shown in Fig. 1(k). Particularly, for h = 4.8 mm, the Type I configuration possesses a double-well potential with the depth of ΔU_1 = 0.204 mJ (Fig. 1(d)), while the Type II configuration possesses a single-well potential (Fig. 1(h)). The combination of these two configurations forms a triple-well potential with a shallower depth, i.e., ΔU_2 = 0.151 mJ, which can reduce the threshold of excitation levels for interwell motions.

On the other hand, the present design, having a triple-well potential, takes the advantage for harvesting energy, such as higher harvesting efficiency and wider operating bandwidth with lower frequencies [14, 37]. When the combined configuration operates in a horizontal direction, a separation distance, d_s, can be set up between the sliding magnets and linear springs. With the increase of d_s, a quadruple-well potential arises from 0 to 6.4 $\times 10^{-2}$ mm, as shown in Fig. 1(n), in which the negative value of d_s denotes that both springs can be compressed by the sliding magnets at the initial stage. In the case of d_s = 0.045 mm, the well depth of the quadruple-well potential is only 0.042 mJ (see Fig. 1(o)), which is much less than that of the triple-well potential in the horizontal configuration. By adjusting the separation distance, the potential energy of the combined configuration can be further distributed more uniformly, which can also provide an outlet for the potential energy imbalance due to the assembly error.

2.2. Working principle of the present energy harvester

Based on the combined configuration of the present harvester, an array-based electromagnetic generator (EMG), a frequency-up-converted piezoelectric generator (PEG), a contact-separation and a freestanding mode triboelectric nanogenerators (TENG-CS and TENG-F) were integrated into a multi-stable mechanical system as harvester units, as schematically presented in Fig. 2(a). The EMG unit consists of a rectangular-shaped magnet array structure with an outer frame as a slider (also as an inertial mass). Two small magnets and copper (Cu) coils fixed to the harvester housing are placed in the air gap that separates the magnet arrays and frames. Each magnet array consists of three block magnets with spacers in between to increase the magnetic field strength across the plane facing the magnets. For the frequency-up-converted PEG unit, the slider is clamped by two folded springs, each of them consists of one thick beryllium bronze beam and five bimorph piezoelectric beams folding on top of each other. One end of the outmost piezoelectric beam is fixed to the harvester housing while the thick metal beam adjacent to the slider with an 80-μm gap. For the TENG unit, the left and right sides of the sliding frame were fabricated by a printed-circuit-board (PCB). The substrate is glass epoxy with a thickness of 1.2 mm. Four parallel arrayed electrodes of Cu were patterned onto the surface of the substrate. Two rectangular-shaped PCBs with a power management circuit on the outer surface and eleven parallel arrayed Cu electrodes on the inner surface were embedded into the harvester housing as left and right sidewalls. Fluorinated Ethylene Propylene (FEP) films with a thickness of 80 μm were attached to the Cu electrodes on sidewalls and both ends of the slider, it can serve as a triboelectric material that contains negative triboelectric charges. A photograph of the fully

assembled prototype is shown in Fig. 2(b). The major fabrication steps for the prototype are depicted in Fig. 2(c). More details regarding the fabrication procedures of this prototype are described in the experimental section.

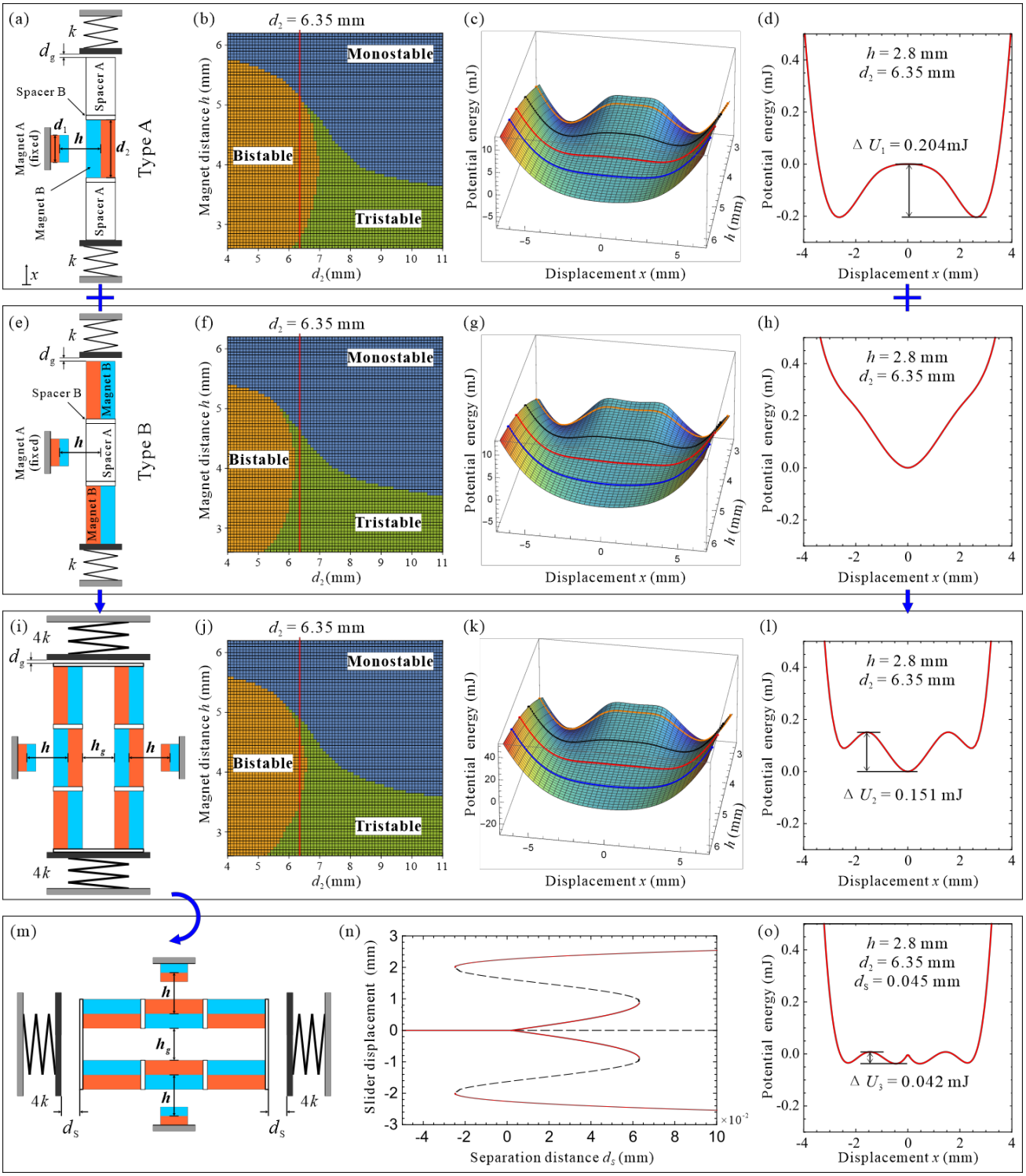

Fig. 1. Schematic of the multi-stable oscillators: structural diagram of (a) configuration Type I and (e) configuration Type II; (b, f, j) numerically categorized different types of stability on the parametric plane; (c, g , k) potential energy varies with separation distance h; (d, h, l, o) the potential energy

functions under the specified parameters; and (n) the bifurcation diagram of equilibrium solutions, the thin lines and dotted lines denote the stable and unstable equilibria, respectively.

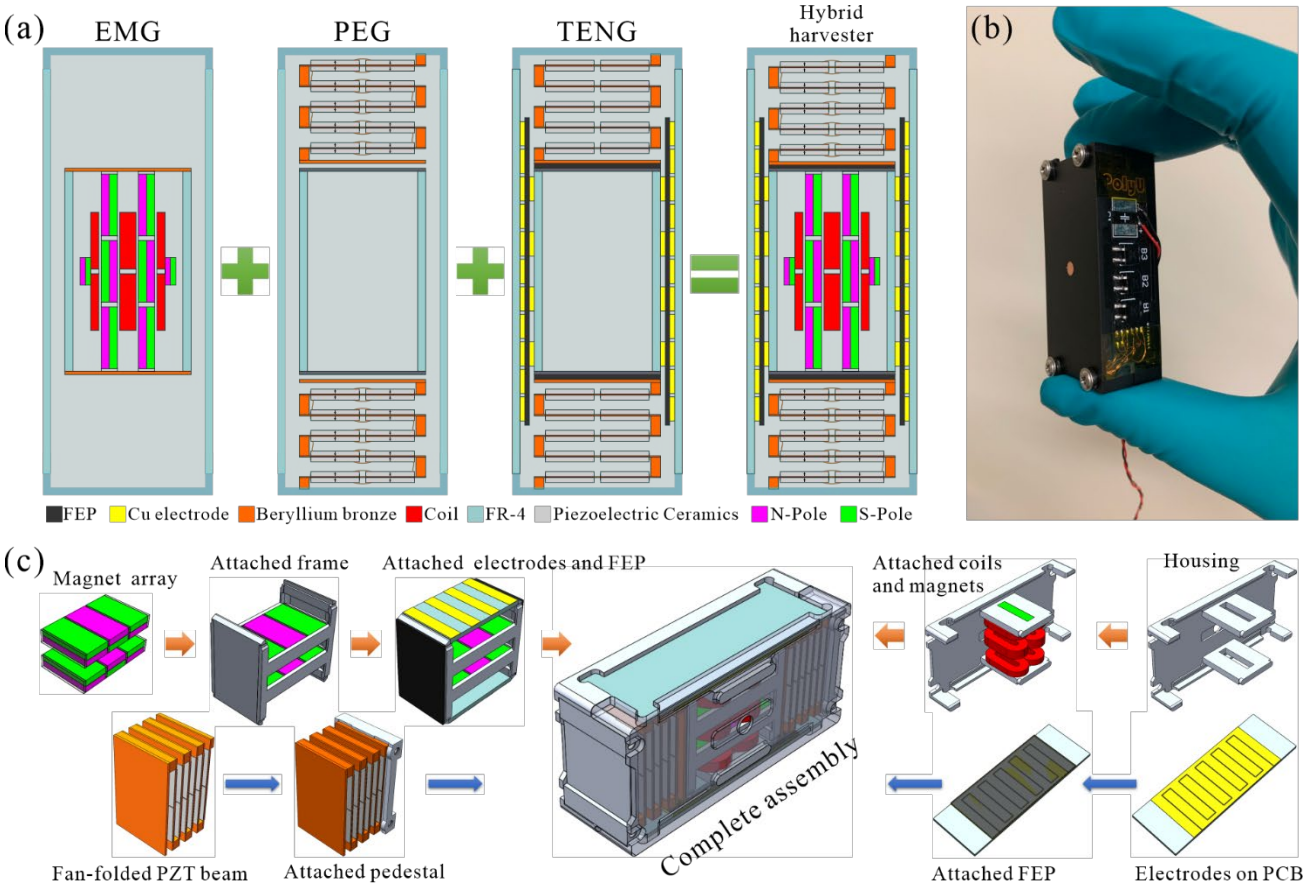

Fig. 2. (a) Schematic of the proposed piezoelectric-electromagnetic-triboelectric hybrid energy harvester. (b) Photograph of the fully packaged prototype. (c) Major fabrication steps toward the assembly of the prototype.

Fig. 3 illustrates the operating principle of the hybrid energy harvester, which can be divided into three parts: the electromagnetic part, the piezoelectric part and the triboelectric part (including a sliding mode and a contact-separation mode). When an external excitation is applied in the working direction of the harvester, the slider (proof mass) starts to oscillate between the both sided walls (TENG-F) and contact, compress and separate from the folded springs alternately (TENG-CS and PEG). For the triboelectric part, the contact areas between the slider, both folded piezoelectric springs and sidewalls of the harvester housing are significant, which result in an electrostatic induction when surface contact occurs. According to the triboelectric series, Cu has a lower electron affinity than FEP, leading to positive triboelectric charges at the Cu surface and negative triboelectric charges at the FEP surface. At initial stage (stage I), the slider locates in the middle position, the beryllium bronze electrodes of two folded piezoelectric springs have the same potential without transferring charges between them. Meanwhile, the Cu electrodes on the slider overlap one group of electrodes on sidewalls in a state of

electrical equilibrium. As the slider moves to the right side (stage II), for the TENG-F unit, the Cu electrodes on the slider leave the overlapping state, electrons flow from the leaving electrodes to the forward electrodes due to the potential drop, and consequently generating triboelectric current through the external connection between the electrode groups. Meanwhile, for the TENG-CS unit, the triboelectric layer on the left side starts to separate from the Cu electrode, while the triboelectric charges are retained on the surfaces, resulting in a potential difference between the FEP film and beryllium bronze electrode. This potential difference drives induced electrons to flow from the right electrode to the left electrode, generating a triboelectric current to the right.

For the PEG unit, the moving slider compresses the right folded spring, causes internal strain in the PZT sheet, yields opposite piezoelectric potential on both sides, and eventually generates electric current from the external circuit. The moving magnetic slider also changes the magnetic flux across the coils, resulting in induced current in the series connected coils of the EMG unit. The triboelectric, piezoelectric, and electromagnetic currents last until the slider reaches to the maximum displacement (stage III). Subsequently, as the slider moves reversely (stage IV), for the TENG-F unit, electrons flow from the leaving electrodes to the forward electrodes, generating an opposite current from stage II. For the TENG-CS unit, the triboelectric potential on the left beryllium bronze electrode increases with the slider gets closer. Positive charges flow back from the right beryllium bronze electrode to the left one. Meanwhile, the release of the internal strain in the PZT sheets and the change of the magnetic flux across the coils can generate an opposite current from stage II. Then, the slider reverts to stage I and repeats the above processes on the other side. Then, the current can be constantly generated by all these units.

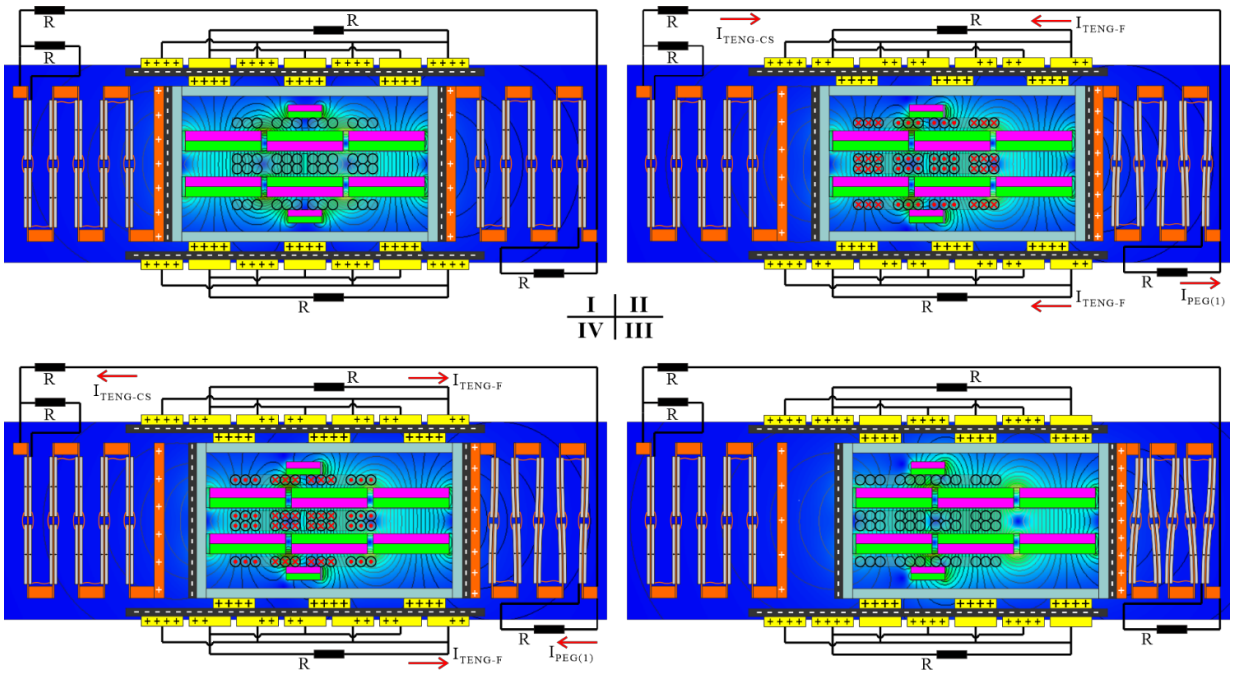

Fig. 3. Working principle of the hybrid energy harvester in a half cycle.

2.3. Theoretical modeling

Two simplified mechanical system models of the hybrid energy harvester in the horizontal and vertical directions are presented in Fig. 4. When an input excitation ($x_b(t)$) is applied to the harvester, the magnetic slider (M) will oscillate with a relative displacement of $x_r(t)$ with respect to the harvester. At the initial stage, there is a separation gap (d_s) between the slider and folded piezoelectric spring(s). Turning to the vertical orientation, $d_s = Mg/k$ where g is the gravitational acceleration and k is the stiffness of the folded piezoelectric spring.

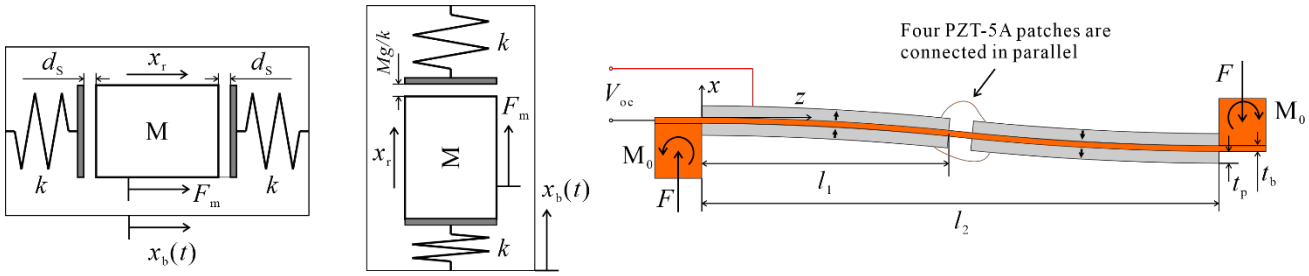

Fig. 4. Mechanical models of the proposed energy harvester in (a) horizontal and (b) vertical directions, respectively. (c) An equivalent mechanical model of one bimorph piezoelectric beam in the folded piezoelectric spring.

In the case of impact with the folded piezoelectric springs, different types of forces are exerted on the slider, namely gravitational force, magnetic force, coulomb's friction force, viscous friction force, and impact force. According to the Newton second law of motion, the governing equations of the mechanical systems in the horizontal and vertical directions are, respectively, given by

$$M\ddot{x}_r + (C_i + C_v + C_e)\dot{x}_r + k_e(|x_r| - d_S) + F_m + \frac{\dot{x}_r}{|\dot{x}_r|}\mu F_l = -M\ddot{x}_b \tag{1}$$

$$M\ddot{x}_r + (C_i + C_v + C_e)\dot{x}_r + kx_r + F_m + \frac{\dot{x}_r}{|\dot{x}_r|}\mu F_l = -M\ddot{x}_b \tag{2}$$

where μ is the coefficients of the dry friction. F_m and F_l are the magnetic force and lateral pressure acting on the slider, respectively. C_i is the additional damping coefficient when the slider is in contact with the folded piezoelectric spring, C_v is the linear viscous damping coefficient, and C_e is the electrical damping coefficient that depends on the following electromagnetic parameters

$$C_e = \frac{(d\varphi / dx_r)^2}{R_L + R_C} \tag{3}$$

where φ is the total magnetic flux across the coils, $d\varphi/dx_r$ denotes the change rate of the magnetic flux with the relative displacement. R_L and R_C are the resistance of the external load and the coils, respectively. Moreover, the effective stiffness of the folded piezoelectric springs, k_e, takes the value of k during impact and zero when they are not during impact, then

$$k_e = \begin{cases} -k,\ x_r < -d_s \\ 0,\ -d_s \le x \le d_s \\ k,\ x > d_s \end{cases} \tag{4}$$

For the PEG unit, consider the symmetry of the folded piezoelectric spring, an equivalent mechanical model of one bimorph piezoelectric beam shown in Fig. 3(b) can be used to simplify complicated calculations. The bimorph piezoelectric beam consists of a beryllium bronze substrate with Young's modulus E_s, effective length l_2, width w, and thickness t_s. Four PZT-5A patches, with Young's modulus E_p, length l_1, width w, and thickness t_p, are attached on the upper and lower surfaces of the beryllium bronze layer and connected in parallel. Let the z-axis be along the length direction, with z = 0 located at the left end. While the x-axis is along the thickness direction, with $x = 0$ at the upper surface of the beryllium bronze substrate. According to the vibration mode and symmetry of the structure, one obtains

$$\frac{Fl_2}{2} - M_0 = 0 \tag{5}$$

Then, the radius of curvature $R(z)$ of the beam at location z can be expressed as

$$\left|\frac{1}{R(z)}\right| = \frac{M(z)}{wD} = \frac{F(l_2 - 2z)}{2wD} \tag{6}$$

where $M(z)$ is the bending moment at z, and D is the bending modulus per unit width of the beam that can be obtained as

$$D = \begin{cases} \frac{E_s t_s^3}{12} + \frac{E_p t_s}{6}(4\,t_p^2 + 6t_s t_p + 3t_p^2),\ z < l_1 \ or\ z > l_2 - l_1 \\ \frac{E_s t_s^3}{12},\ l_1 < z < l_2 - l_1 \end{cases} \tag{7}$$

Due to the structural symmetry, the position of the neutral axis is given by

$$t_n = -\frac{t_s}{2} \tag{8}$$

Then, the lateral stress on the PZT-5A patches at the position (z, x) can be written as

$$\sigma(z,x) = \left|\frac{1}{R(z)}\right|(x - t_n)E_p = \frac{FE_p}{2wD}(l_2 - 2z)(x - t_n) \tag{9}$$

The induced electric field $E(z, x)$ in the thickness direction at (z, x) on the PZT-5A patches is

$$E(z,x) = \left(\frac{-d_{31}}{\varepsilon_r \varepsilon_0}\right) \times \sigma(z,x) = -\frac{d_{31} FE_p}{2\varepsilon_r \varepsilon_0 wD}(l_2 - 2z)(x - t_n) \tag{10}$$

where d_{31}, ε_0, and ε_r are the piezoelectric strain constant, the permittivity of free space, and the dielectric constant of PZT-5A, respectively. Hence, the generated open-circuit voltage of the PEG unit can be given by

$$V_{oc-PEG} = \frac{1}{l_1}\int_0^{l_1}\int_0^{t_p} E(z,x)dxdz = -\frac{d_{31}FE_p t_p l_1}{4\varepsilon_r\varepsilon_0 wD}(t_s + t_p)(l_2 - l_1) \tag{11}$$

For the EMG unit, as described by Faraday's Law of electromagnetic induction, the relationship of the open-circuit voltage V_{oc} and the short-circuit current I_{sc} is presented as

$$V_{oc-EMG} = -N\frac{d\varphi}{dt} \tag{12}$$

where N is the effective number of turns of the coil group.

For the TENG-F unit, V_{oc} can be expressed as follows [38]

$$V_{oc-F} = \frac{Q_{sc}}{C(x_r)} = \frac{\Delta S \cdot \sigma}{C(x_r)} \tag{13}$$

where Q_{sc}, $C(x_r)$, and σ are the short-circuit transferred charge, the capacitance between two electrodes with respect to the displacement, and the surface charge density on the slider, respectively. Since the transferred charge is induced by the triboelectric charge on the slider, the potential difference between the two group of electrodes is proportional to the change of contact area, ΔS. While for the TENG-CS unit, the generated output voltage can be obtained by the *V-Q-x* relationship for the metal-freestanding-layers, which is expressed by [39]

$$V_{oc-CS} = \frac{\sigma_{CS} x_r}{\varepsilon_0} \tag{14}$$

where σ_{CS} is the surface charge density on the folded piezoelectric spring electrodes.

2.4. Performance characterization

Based on the derived governing models, we conducted a numerical analysis in this section to characterize the dynamic behaviour before experiment verification. Firstly, a static experimental test was carried out to obtain the nonlinear coefficients of the restoring force for establishing the potential energy functions of the proposed energy harvester in both tri-stable and quad-stable modes, respectively. As shown in Fig. 5(a), a force acting on the magnetic slider was measured at different displacements by using a digital force gauge. Fig. 5(b) shows the variation of the restoring force with the displacement of the magnetic slider. Then, the fitted polynomial expressions for the restoring forces of both tri-stable and quad-stable modes can be, respectively, written as:

$$F_{\text{tri}} = 415.172x_r - 2.405\times10^{8}x_r^3 + 3.630\times10^{13}x_r^5 - 1.249\times10^{18}x_r^7 \tag{19}$$

$$F_{\text{quad}} = \begin{cases} -424.827x_r - 2.405\times10^{8}x_r^3 + 3.630\times10^{13}x_r^5 - 1.249\times10^{18}x_r^7, & |x_r| < 1.1\times10^{-4} \\ -9.460\times10^{-2}\,\text{sgn}(x_r) + 435.172x_r - 2.405\times10^{8}x_r^3 + 3.630\times10^{13}x_r^5 - 1.249\times10^{18}x_r^7, & |x_r| > 1.1\times10^{-4} \end{cases} \tag{20}$$

From the potential energy diagram (Fig. 5(c)), it is obvious that the quad-stable system has lower potential energy than that of the tri-stable one. This implies the quad-stable system may require a lower excitation level to pass through potential wells than the tri-stable one. However, the outmost potential wells in the quad-stable mode are deeper than the one in the tri-stable mode, resulting in a higher local oscillation frequency in the quad-stable mode [15, 40]. In addition, the folded piezoelectric spring has an equivalent stiffness of ~3.12×10^3 N/m and a natural frequency of 173 Hz. By coupling a strong magnetic force, the maximum restoring force of the multi-stable system is lower than 0.21 N in the displacement range of –2.5 to 2.5 mm. Consequently, the output performance of the PEG unit can be improved under low-frequency and low-intensity vibrations.

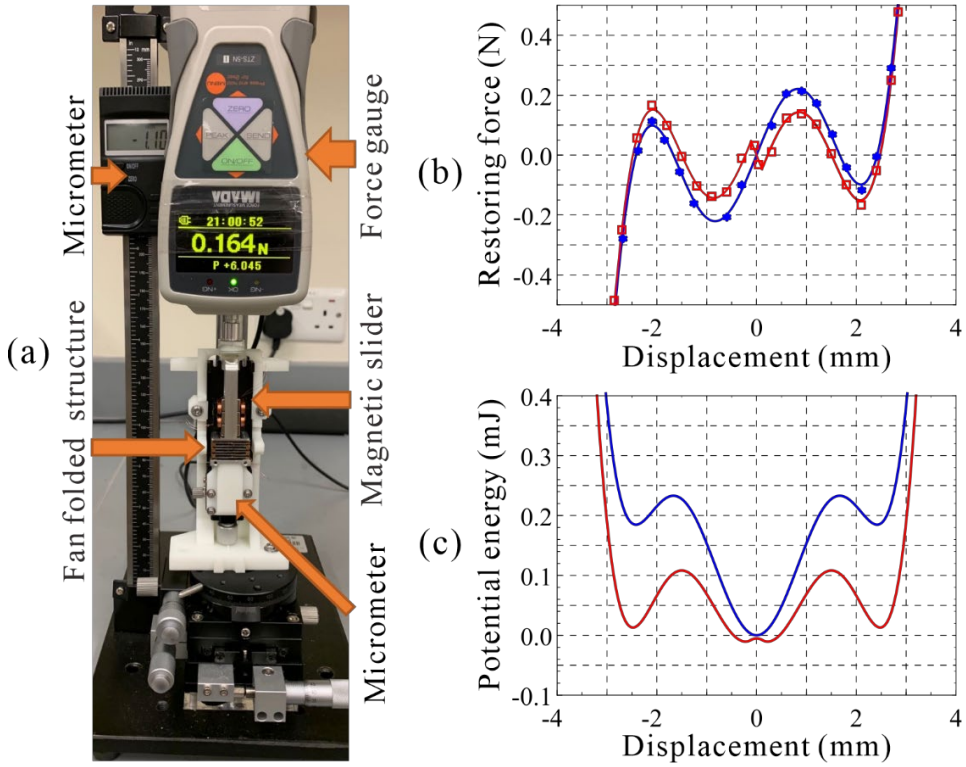

Fig. 5. (a) Experimental setup for measuring the restoring force. (b) Variation of the restoring force with displacement. (c) Potential energy functions of the tri-stable and quad-stable systems.

Fig. 6 shows the amplitude-frequency responses and its corresponding phase planes of the tri-stable and quad-stable systems at different constant frequency excitations (from 1 to 20 Hz) with 1 g acceleration, respectively. The points in the figure denote the amplitude of the displacement response at the corresponding frequency in one excitation cycle, while the multiple points at one frequency represent the occurrence of a period-doubling/chaotic motion. As shown in Fig. 6(a), the tri-stable

system oscillates with a large-amplitude of inter-well motions from the starting frequency of 1 Hz to the cut-off frequency of 11.6 Hz. This shows the performance of period-doubling behaviour at low frequencies. After the cut-off frequency, the tri-stable system exhibits a chaotic motion with a relatively small amplitude in the frequency range of 11.6–15.8 Hz. In contrast, the quad-stable system can perform large-amplitude inter-well oscillations in a wider frequency range of 1–12.3 Hz, and the corresponding chaotic motion (in the range of 11.6–16.1 Hz) exhibits large-amplitude oscillations, leading to a better energy harvesting efficiency than that in the tri-stable system.

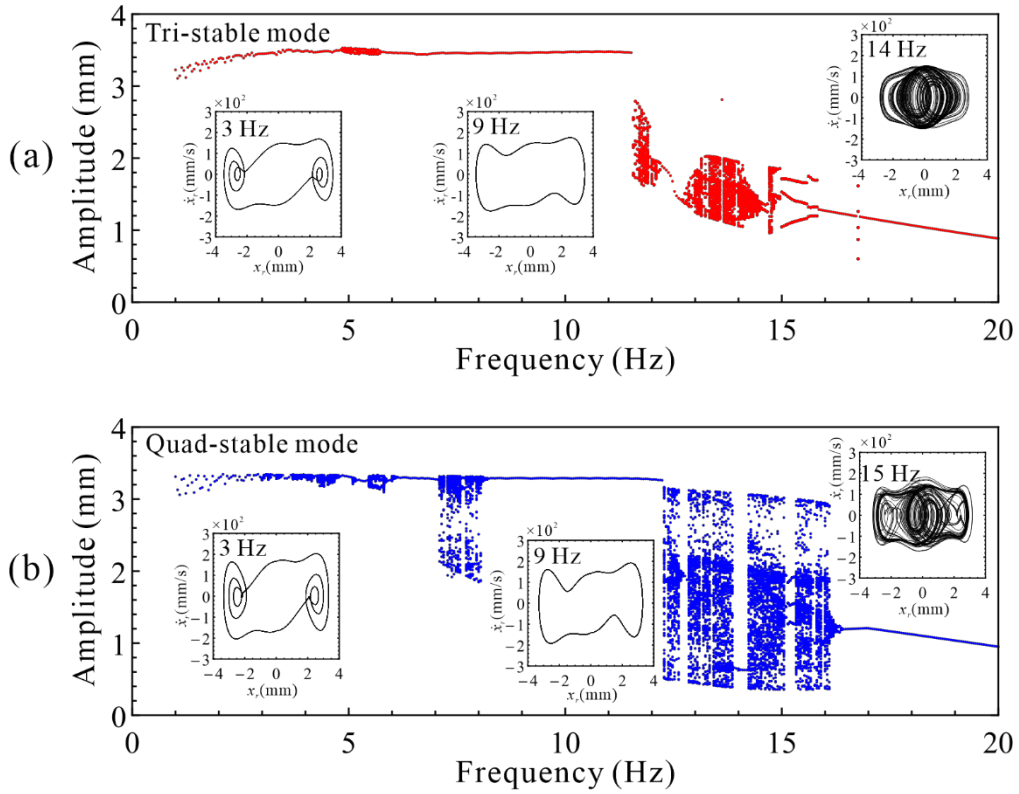

Fig.6. Simulated amplitude-frequency responses and corresponding phase portraits of the (a) tri-stable and (b) quad-stable modes under various frequency excitations with 1 g acceleration.

The starting-up processes of the tri-stable and quad-stable systems are investigated under a sinusoidal excitation at 3 Hz as shown in Fig. 7. The acceleration amplitude is changed from 0.1 g to 1.5 g. In the tri-stable system (Fig. 7(a)), the slider is trapped in the middle potential well at stage I (0.1–0.48 g), and can only perform small-amplitude intra-well oscillations, as shown in the time-varying phase diagram accordingly. With the acceleration amplitude increases over 0.48 g, the slider is activated into inter-well oscillations after an amplitude jumping phenomenon. The displacement amplitude continues to enlarge as the excitation level increases. In the quad-stable system (Fig. 7(b)), at the very beginning of stage I (0.1–0.52 g), the slider can only perform small-amplitude intra-well oscillations in one of the middle potential wells. As the acceleration amplitude increases to 0.19 g, the slider begins to oscillate between the two middle potential wells after a small amplitude jumping. When the acceleration amplitude further increases to 0.52–0.62 g, the slider can jump out of the two

middle potential wells but be trapped in the one of the outer wells as shown in the phase diagram, due to the deeper outer well depth and higher local oscillation frequencies. After the acceleration amplitude increases over 0.62 g, the slider passes through a chaotic region and finally enters into large-amplitude inter-well oscillations. The above starting-up processes and phase diagrams clearly illustrate that the large-amplitude motions of the tri-stable and quad-stable systems are highly dependent on the level of input excitations. Particularly, even though the potential wells of the quad-stable system are globally shallower than that of the tri-stable one, its threshold of inter-well oscillation motions is higher than that of the tri-stable one under the low-frequency sinusoidal excitation of 3 Hz, due to the higher local oscillation frequencies of the outer wells.

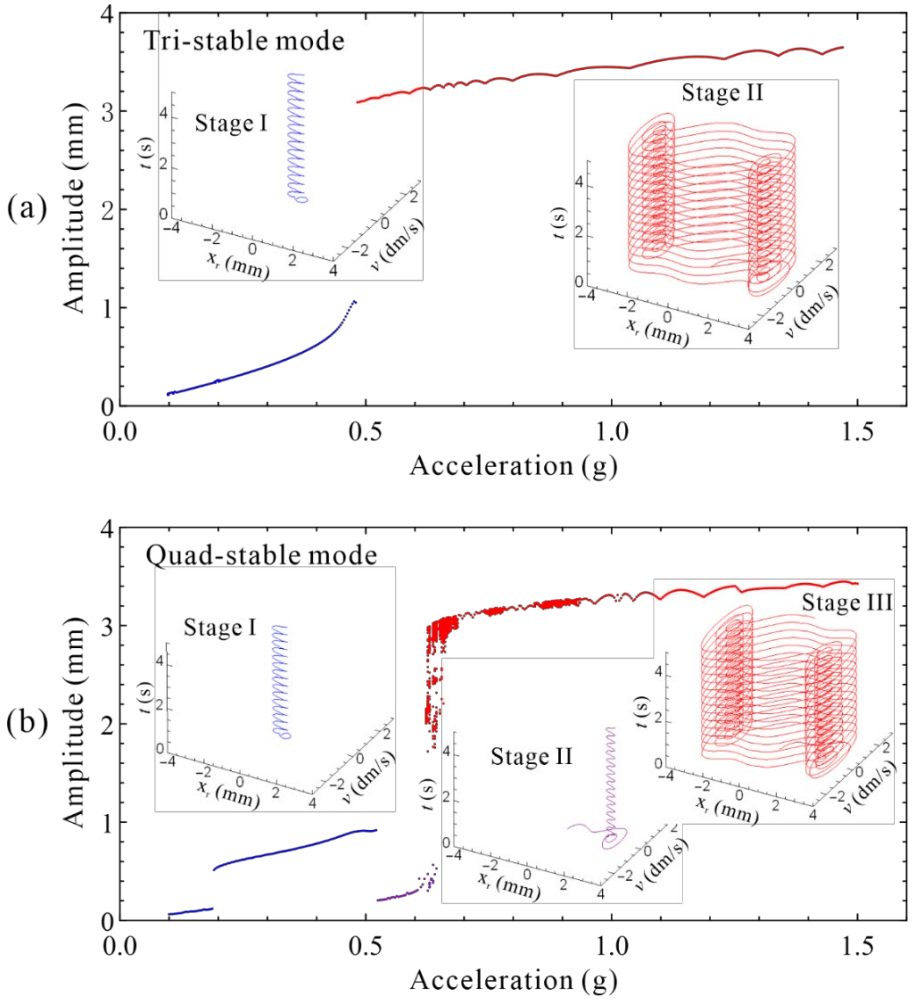

Fig.7. Starting-up processes of (a) the tri-stable mode and (b) the quad-stable mode under a sinusoidal excitation of 3 Hz.

3. Results and discussion

3.1. Prototype fabrication and experimental setup

To verify the performance of the proposed energy harvester, a miniaturized prototype was fabricated and tested under different excitation levels. Photographs of the fabricated prototype before assembling components are presented in Fig. 8(a). The fabricated prototype consisted of two aluminum alloy housing structures with dimensions of 1.8 × 2 × 6 cm^3. A dual magnet-array was fixed by a beryllium bronze frame (2.86 × 2.19 × 1.43 cm^3). Each magnet-array (2 × 1.27 × 0.3 cm^3) was composed of three NdFeB (N35 grade) block magnets with two acrylic spacers (1.27 × 0.3 × 0.05 cm^3) in between. Each copper coil was wound into an ellipse shape (1.3 × 0.6 × 0.2 cm^3), in a position facing the magnet-array. An air gap of 0.3 mm between the magnet-array and coil surface was maintained. Each six-beam-fan-folded structure (2.06 × 1.33 × 1.21 cm^3) was mounted on an aluminum alloy pedestal, which can be fixed to the housing structure by bolted connections. Each beam (2 × 1.33 cm^2) consisted of a 0.3 mm thick beryllium bronze substrate and four 0.13 mm thick piezoelectric patches (PSI-5A4E PZT) supplied by PIEZO SYSTEMS, INC. The links (1.33 × 0.2 × 0.15 cm^3) made of phosphor bronze can be used to connect the beams. Two PCBs with one side etched into the parallel arrayed electrodes and the other side as a rectifying circuit were inserted into the housing structure. FEP films were attached on the parallel arrayed electrodes and the top surface of the fan-folded structure to act as a triboelectric material.

Fig. 8(b) shows the stable equilibrium positions of the fabricated prototype in the vertical (tri-stable) and horizontal (quad-stable) directions, respectively. The experimental setup for testing the fabricated prototype is illustrated in Fig. 8(c). In this setup, the prototype was mounted on an electrodynamic shaker (SPEKTRA APS 113) that can generate a harmonic base excitation in horizontal and vertical directions with various frequencies and accelerations (Fig. 8(d)). The shaker was powered by an amplifier (SPEKTRA APS 125) in conjunction with a signal generator (Keysight 33500B) to provide different operating frequencies to the shaker, while the base acceleration can be monitored by using a reference accelerometer (Dytran 3093M10) connecting to an IEPE acceleration sensor amplifier (MonoDAQ MONODAQ-E-ACC-1). The output terminals of all harvester units were connected to the probe of a digital oscilloscope (Keysight DSOX3014T), which can record and display the output voltage of each harvester unit across a load resistor or in an open circuit.

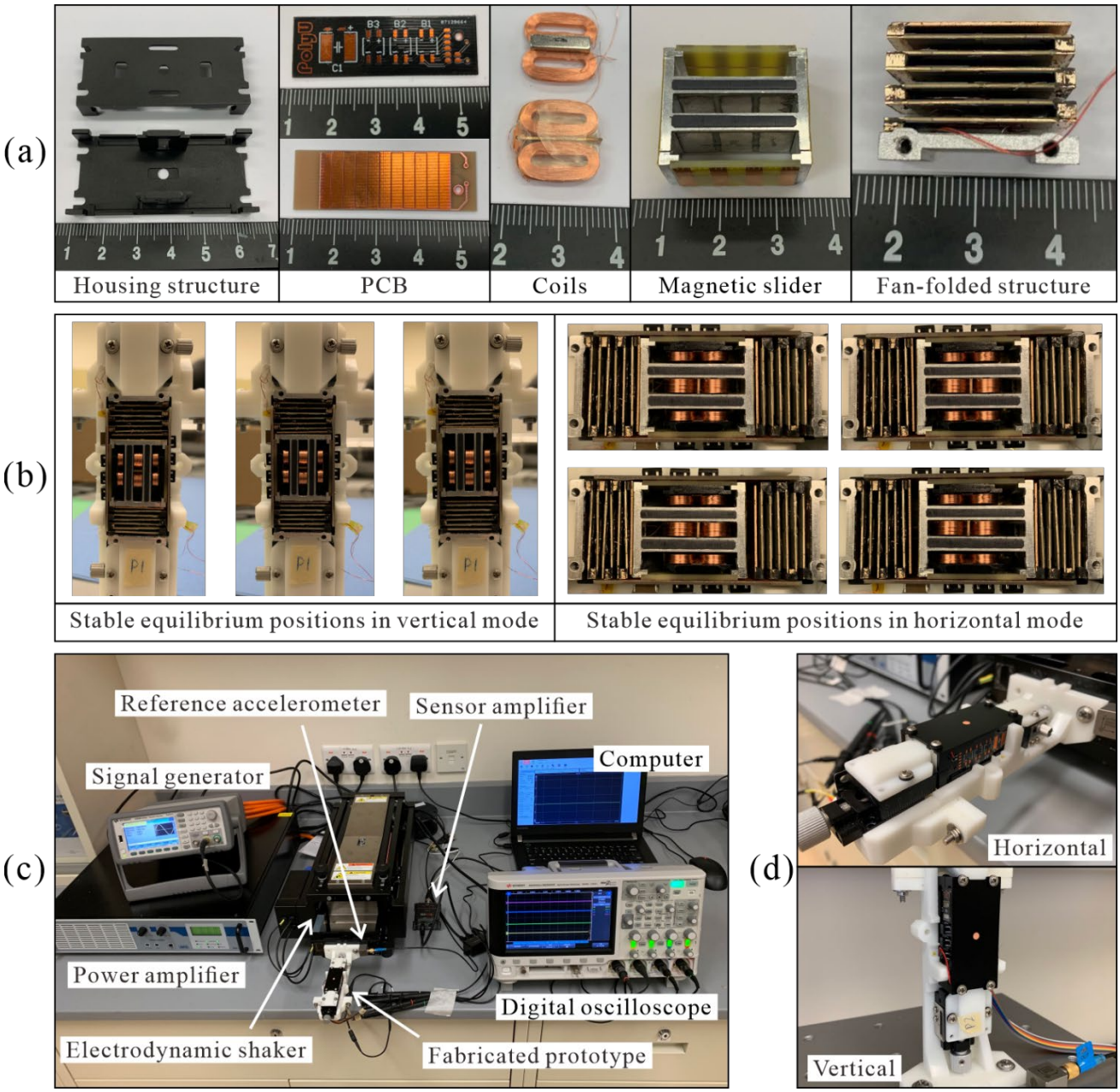

Fig. 8. (a) Photographs of the fabricated prototype before assembling components. (b) Stable equilibrium positions for the fabricated prototype in both horizontal and vertical modes, respectively. (c) Schematic of the experimental setup for testing the fabricated prototype. (d) The prototype mounted on an electrodynamic shaker in horizontal and vertical orientations, respectively.

3.2 Harmonic excitation tests

Under a sinusoidal acceleration with various acceleration amplitudes (0.5 g, 1 g, and 1.5 g), the frequency responses of various harvester units in the tri-stable (vertical) and quad-stable (horizontal) systems are investigated, respectively. The simulated and experimental open-circuit voltage values of various harvester units in the frequency range of 1–20 Hz are presented in Fig. 9. Because all harvester units in the prototype can be driven by the same mechanical motions, their open-circuit voltage values

show similar broadband responses according to the selected multi-stable nonlinearity mode. In the tri-stable state, as shown in Figs. 9(a)–(e), all harvester units can produce a high voltage output in the bandwidth of ~1 to ~7 Hz under 0.5 g, except for a narrow frequency band around 4 Hz. Under a 4 Hz excitation, the slider can be eventually caught in the outer well of one side, which will disable the TENG-CS and PEG units on the other side (the upper PEG in this experiment). When the excitation level increased to 1 g, the slider can perform large-amplitude inter-well oscillations in the bandwidth of ~1 to ~11 Hz, resulting in high voltage responses in all harvester units. However, the experimental results of TENGs are significantly lower than the predicted ones, because the measuring circuit in experiment cannot reach to an ideal open-circuit state. When the excitation level was set at 1.5 g, the cut-off frequency of all harvester units further increased to ~13 Hz. To compare the relatively stable voltage responses of PEG and TENG-CS, whose open-circuit voltage values linearly depend on the displacement. Both EMG and TENG-F units encountered a sudden drop in voltage during the transition process from a period-doubling/chaotic motion to a periodic motion (i.e., 6–9 Hz). This transition process may cause a change in the form of motion, resulting in the change of velocity distributions and the reduction of voltage responses.

When the prototype was operated at a quad-stable mode, the slider cannot perform large-amplitude inter-well oscillations throughout the excitation level of 0.5 g, as shown in Figs. 9(f)–(i). Only relatively low energy output can be generated by the harvester units when the slider oscillated between the two middle wells at the frequencies between 2–6 Hz and higher than 13 Hz. Note that, for the TENG-CS unit, the intra-well oscillation of the slider in the outer well (i.e., 1–2 Hz and 7–12 Hz) may result in a wrong prediction. In the theoretical model of the TENG-CS unit, V_{oc} that is simple linearly depends on the displacement (x_r). Nevertheless, the TENG-CS unit has lost its output properties, because the dielectric surface on the slider cannot make contact with the two electrodes alternately. When the acceleration increased to 1 g, the excitation can activate the large-amplitude inter-well oscillation of the slider in the frequency range of ~1 to ~12 Hz, which is wider than that of the tri-stable mode. Meanwhile, at the low frequencies, the voltage responses of the individual harvester units in the quad-stable state are higher than that in the tri-stable state. When the excitation level further increased to 1.5 g, all harvester units generated large-amplitude voltage responses over a wider range of frequencies (1–16 Hz). In addition, the measured open-circuit voltage levels of the individual harvester units are lower than the calculated ones. This discrepancy is mainly due to the fact that the impact between the slider and the folded piezoelectric springs is elastic and the mass effect of the folded piezoelectric springs is neglected. Indeed, the impact effect cannot be strictly inelastic and the mass effect of the piezoelectric springs can cause a velocity mutation based on the momentum theorem.

Based on the above numerical and experimental results, a tri-stable mode is more easily to be triggered into large-amplitude inter-well motions for generating a higher energy output under a sinusoidal excitation. When the external excitation level is high enough to activate a quad-stable mode

for inter-well motions, it shows superior wideband and low-frequency performance over the tri-stable mode. Furthermore, both nonlinear dynamical modes can offer a high-efficiency operating bandwidth that covers the vibration frequencies of general human motions (1–10 Hz) under 1 g acceleration.

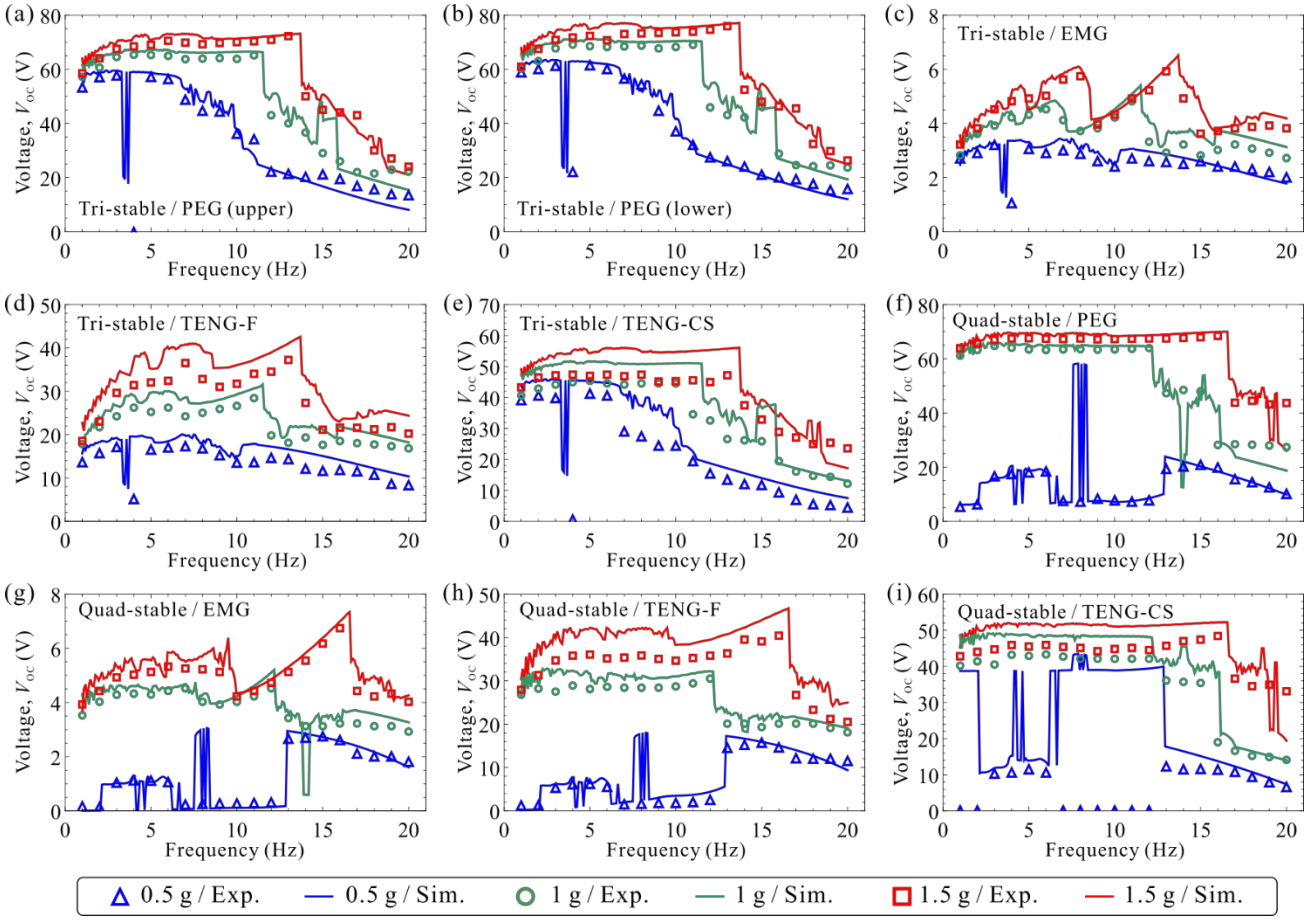

Fig. 9. Open-circuit voltage of various harvester units against different frequencies under 0.5 g, 1 g and 1.5 g for (a)–(e) tri-stable mode; and (f)–(i) quad-stable mode.

To characterize the electrical performance of the individual PEG, EMG, TENG-F and TENG-CS units, the open-circuit voltage, load current, and electrical output versus external load were all measured and calculated under the vibration excitation at 3 Hz with 1 g acceleration. For the PEG unit, a high peak open-circuit voltage of 64.1 V (root-mean-square of peaks over multiple cycles, hereinafter inclusive) can be generated during the compressed stage, as shown in Fig. 10(a). At the released stage, only a relatively small reverse voltage can be generated and would slowly return to zero due to the hysteresis characteristics of piezoceramics. With the increase of load resistance, the maximum power of 35.37 mW was delivered from the PEG unit across an optimum load resistance of 35 kΩ (Fig. 10(b)), corresponding to the maximum current of 0.85 mA (Fig. 10(c)). For the EMG unit, due to the instantaneous change in velocity at the time of impact, a smaller peak occurred at the peak open-circuit voltage of 4.26 V as shown in Fig. 10(d). The obtained maximum power across an optimum load resistance of 210 Ω was 35.08 mW (Fig. 10(e)), while the corresponding maximum current was 12.92

mA (Fig. 10(f)). In Fig. 10(g), the peak open-circuit voltage levels of the TENG-F and TENG-CS units were 27.4 V and 40.3 V, respectively. Under an optimum load resistance of 19 MΩ, the maximum power of the TENG-F unit was 27.12 μW with a maximum load current of 1.19 μA, while the TENG-CS unit can reach to the maximum power of 60.99 μW with a 3.59 μA maximum load current at an optimum load resistance of 17 MΩ (Figs. 10(h) and 10(i)). Among all individual units, the EMG unit can generate a larger output current but with a relatively lower load voltage due to the low internal resistance, whereas the PEGs and TENGs can provide large voltage output levels but with a small current across the load due to their high internal resistance. In addition, the EMG unit can generate a relatively higher power output compared with the individual PEGs and TENGs, but the EMG unit occupies more volume and weight than other units in this prototype. The volume and weight proportions of all individual units are presented in Figs. 10(j) and 10(k).

In Fig. 10, the results show that the PEG units have the highest normalized power density, whether it is calculated based on the volume ratio (7.65 mW cm^{-3}) or weight ratio (2.43 mW g^{-1}). The EMG unit ranks second with the normalized power density of 4.62 mW cm^{-3} and 1.63 mW g^{-1}. For TENGs, even though they account for only 0.65% and 0.51% of the total volume and weight, respectively, their normalized power density is quite low due to the relative-low charge density on the surface of plain FEP. Many methods have been reported to increase the surface charge density of a dielectric material, such as material selection [41], surface modification [42] and contact improvement [43], which could increase the charge density to hundreds of μC m^{-2} and boost the output power tens of times. Furthermore, coupling EMG with PEG and TENG takes good advantages under low frequencies in energy storage. Under an ultra-low frequency excitation, the EMG unit can only provide a low output voltage which might not be sufficient to efficiently drive an electronic load, but the PEG (with FUC approach) and TENG units can achieve a satisfactory output voltage level under such frequencies. This can solve the problem of voltage insufficiency in ultra-low-frequency applications. Storing the harvested energy in a storage unit such as capacitors or rechargeable batteries, the low output voltage of EMG limits the maximum voltage stored in capacitors that can be optimized by hybridizing with the PEG (with the FUC approach) and TENG mechanisms.

It is worth noting that the normalized harvested power density of electromagnetic harvesters grows proportionally to the square of dimensions, but piezoelectric harvesters do not vary with dimensions [44]. Therefore, the proposed energy harvester can be further miniaturized to compare with those existing ones that mainly rely on EMG units. Owing to the full space sharing between PEG and EMG units, there is no need to provide additional space for the mechanical motion of inertia components. Under 1 g sinusoidal acceleration at 3 Hz, the overall normalized power density of 3.69 mW cm^{-3} g^{-2} can be resulted. Note that a considerable amount of volume and weight occupied in the fabricated prototype can be used to adjust the experimental parameters. Excluding the redundant volume and weight will further increase the power density over 10%.

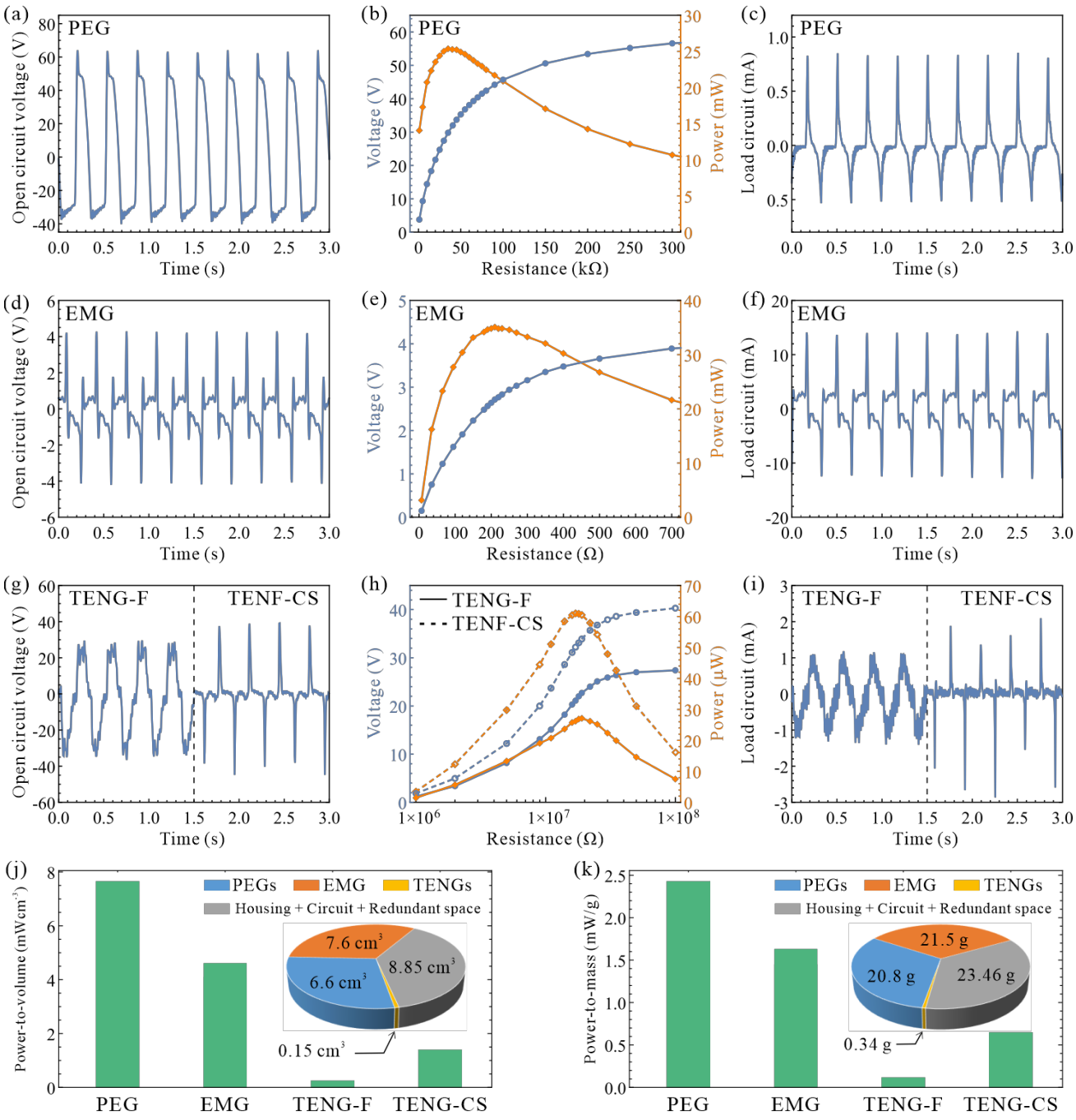

Fig. 10. Measured (a, d, g) open-circuit voltage and (c, f, i) load current for the individual units. (b, e, h) Dependence of the output voltage and maximum power of the individual units on variable external load resistance values. (j) Power-to-volume ratios of the PEG, EMG and TENG units across various optimum loads. (k) Power-to-mass ratios of the PEG, EMG and TENG units. All the results were conducted under 1 g sinusoidal acceleration at 3 Hz in horizontal direction provided by an electrodynamic shaker.

3.3 Human motion tests

To evaluate the energy generation performance of the present energy harvester, a series of experiments were conducted to investigate the capacitor charging behaviour under typical human motions, e.g., walking (5 km/h) and slow running (8 km/h). The fabricated prototype placed horizontally/vertically in a smartphone armband can be attached to arm, wrist, knee and ankle, as shown in Fig. 11(a, e, i, and m) and Video S1. When the harvester units of the prototype are working simultaneously, a rectifier bridge circuit is required for output hybridization to avoid a large internal power consumption [32]. In this work, five bridge rectifier ICs (MB110S) were utilized to convert the AC outputs of each harvester unit into DC signals, and subsequently the rectified outputs were connected in parallel to a 560 μF storage capacitor (Fig. 12(a)). The capacitor charging curves under various human motions were recorded by a digital oscilloscope, and the acceleration levels generated by the human-body-induced vibration were also measured by a 3-axis accelerometer (Dytran 3093M10) simultaneously. The measured 3-axis acceleration waveforms, corresponding to different wearable positions under the walking and slow running motions, are shown in Fig. 11(b, f, j, and n) and Fig. 11(c, g, k, and o), respectively. In these figures, we observe that the slow running motion can generate a higher acceleration level along all the three axes to compare with the walking motion. Moreover, the lower wearable positions (i.e., ankle and knee) generated a higher acceleration level than the upper wearable positions (i.e., wrist and upper-arm). In this case, the fabricated prototype in the horizontal position (with a quad-stable mode) mainly utilized kinetic energy along the *x*- and *y*-axes. While in the vertical position, the fabricated prototype (with a tri-stable mode) mainly depended on the *z*-axis excitation.

Under the walking mode, the acceleration levels along all the three axes at the upper-arm position are lower than 0.5 g with a dominant frequency around 1 Hz. The fabricated prototype can only perform small-amplitude intra-well motions with a low voltage output. After a 64 s walking motion, the 560 μF capacitor can only be charged up to 2.9 and 8.3 V for the horizontal and vertical positions, respectively. Switching to the slow running mode, the peak acceleration levels along the *x*- and *z*-axes at the upper-arm position are higher than 1 g with the dominant frequencies of 1.5 and 2.4 Hz, respectively. The fabricated prototype can successfully perform large-amplitude inter-well motions and the 560 μF capacitor can be charged up to 16 and 23.7 V for the horizontal and vertical positions, respectively. At the wrist position, the acceleration levels along *x*- and *z*-axes under walking motions are similar. Both of them are over 0.8 g with the dominant frequencies of 1 and 1.5 Hz, respectively. Therefore, the 560 μF capacitor can be charged up to a similar level of 14.1 and 13.8 V for the horizontal and vertical positions, respectively. The vertical case shows a quicker charging rate at the early stage due to the higher working frequency, while the horizontal case performs a better long-term charging rate due to the higher voltage output at low frequencies. Under the slow running motion, the peak-to-peak acceleration levels at the wrist position increased to about 5 g and 3.5 g along the *x*- and *z*-axes with a dominant frequency of 2.4 and 1.5 Hz, respectively. These results show 22.1 and 19.2 V

on the 560 μF capacitor for horizontal and vertical cases, respectively. For the lower wearable positions, the fabricated prototype is capable of performing large-amplitude inter-well motions under both walking and slow running motions. After a charging time of 64 s, all the cases can charge the 560 μF capacitor up to over 18 V (see Figs. 11((l) and (p)).

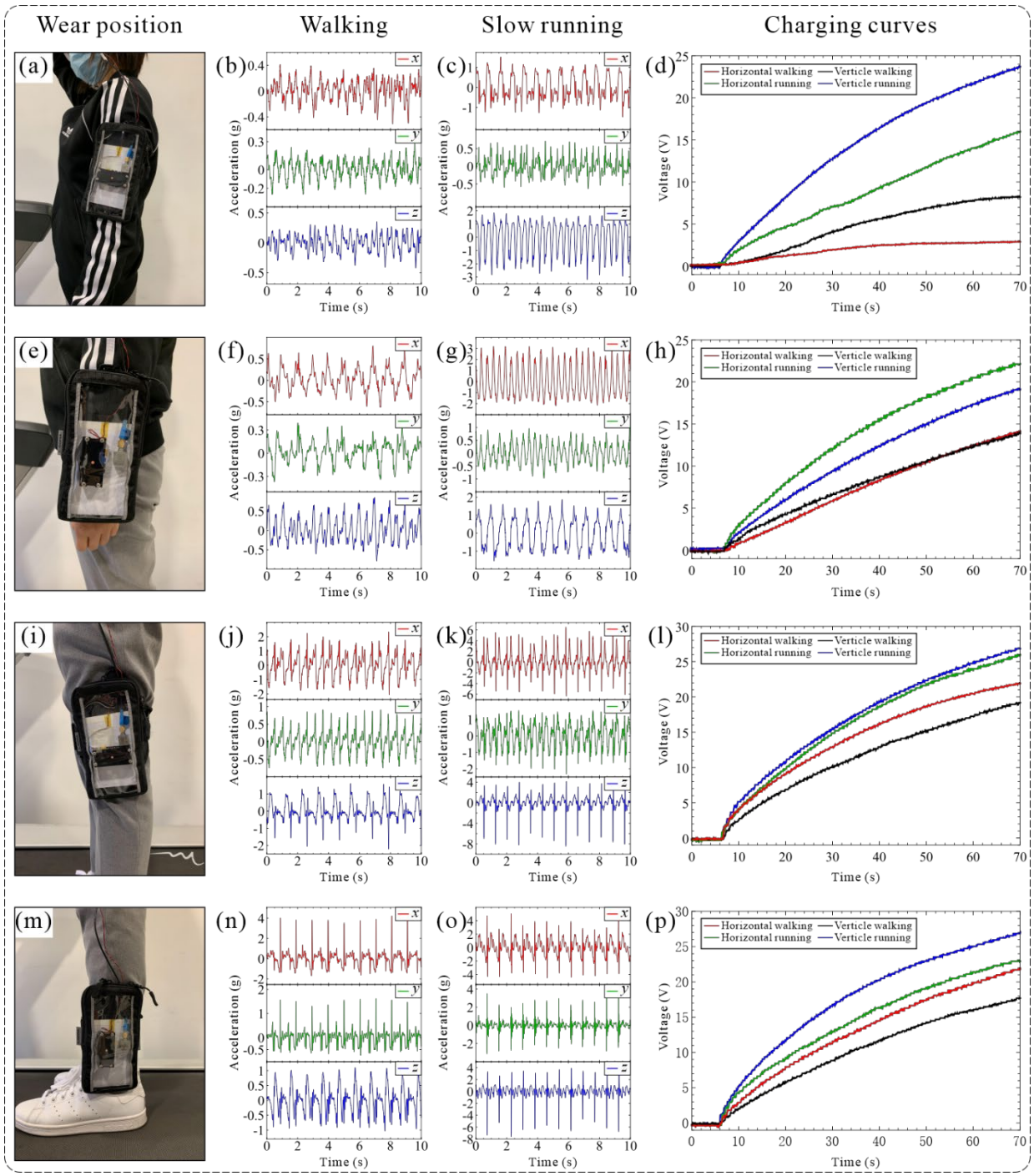

Fig. 11. The energy harvesting capability of the proposed energy harvester under various human body-induced vibrations. (a, e, i, and m) Photographs of the human motions on a treadmill with the prototype placed at different wearable positions. (b, f, j, and n) Measured acceleration waveforms in walking motions with the prototype placed at different wearable positions. (c, g, k, and o) Measured

acceleration waveforms in slow running motions with the prototype placed at different wearable positions.

3.4. Application to electronic devices

To verify the potential of the tri-hybrid energy harvester as an efficient power source for practical applications, the fabricated prototype was used to power up several commercial electronics by harvesting human-induced biomechanical energy. In these demonstrations, five full-bridge rectifiers (MB110S) were employed to convert AC electrical power into DC signals, and then the rectified electricity was collected in a storage capacitor (C) with commercial electronic(s) connected in parallel (Fig. 12(a)). Fig. 12(b) shows the charging curves of a 560 μF capacitor charged by the individual harvester units and hybrid harvester at 3 Hz under 1 g acceleration. The capacitor charging characteristic of the hybrid harvester shows superior performance over any individual harvester units. The capacitor charging process can be divided into two stages: a turbulent charging stage and a trickle charging stage. At the turbulent charging stage, the charging curve of the EMG unit increases rapidly early on and quickly becomes saturated due to its high current output effect. However, both PEGs and TENGs perform much better at the trickle charging stage due to their high voltage output but very low current output effects. The charging speed of the TENGs is much lower than that of the PEGs and EMG but maintains high consistency.

The demonstration of powering three electronic thermohygrometers simultaneously using the fabricated prototype worn on the wrist during walking motion is shown in Fig. 12(b) and Video S2. In the demonstration, the charging characteristics of a 470 μF storage capacitor connected in parallel with the three electronic thermohygrometers are shown in Figs. 12(c) and 12(d). It can be observed that these thermohygrometers can be turned on when the storage capacitor is up to 1.3 V after 8 s. However, due to the unstable trigger of inter-well motions under this excitation level, it can induce the fluctuation of the supply voltage. Sometimes, an excessive supply voltage level will cause an abnormal display on the electronic thermohygrometers. Therefore, a Zener diode was connected in parallel with the electronic thermohygrometers to maintain the supply voltage below 2 V. In addition, by handshaking, the present harvester can successfully brighten 296 LEDs (Fig. 12(e) and Video S3) and power up 20 electronic thermohygrometers simultaneously (Fig. 12(f) and Video S4).

A performance comparison between the proposed energy harvester and those recently reported hybrid energy harvesters is presented in Table 1. The present device shows outstanding performance compared with other devices in terms of the operation bandwidth and normalized power density at low frequencies. The multi-stable nonlinear mechanism performs well in biomechanical energy harvesting applications, and it offers a high-efficiency operating bandwidth that can cover the vibration frequencies of general human motions. In terms of durability, no significant damage of the fan-folded beams or magnetic slider is observed under a long period of experimental time.

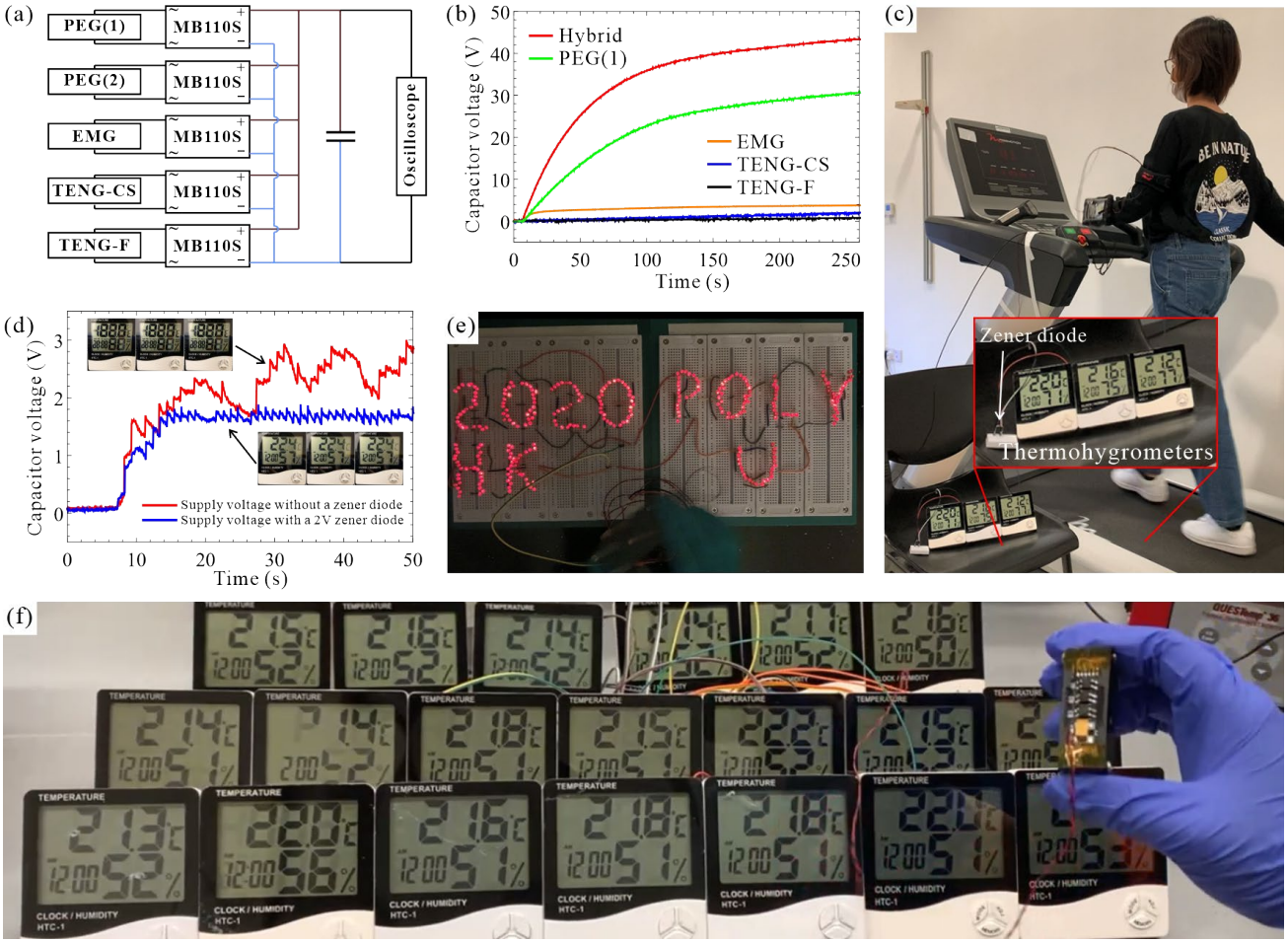

Fig. 12. (a) Demonstration of the proposed energy harvester as a portable power source for practical applications. (b) Capacitor charging characteristics of the PEGs, EMG, TENGs and hybrid energy harvester at 3 Hz under 1 g acceleration. (c) Photograph of three electronic thermohygrometers powered by the fabricated prototype worn on the wrist under walking (5 km/h) on a treadmill. (d) Charging curves of a 470 μF capacitor while driving three electronic thermohygrometers connected in parallel with and without a Zener diode. (e) Photograph of 296 LEDs driven simultaneously using the prototype under fast handshaking motions. (f) Photograph of 20 thermohygrometers powered by the prototype under slow handshaking motions.

Table 1 Comparison of the proposed tri-hybrid energy harvester with similar works reported recently.

Reference (Working Modes*)	Operating Conditions	Normalized Power Density
Ref. [17] (PE + EM + TE)	2–12.5 Hz, 1 g	1.97 mW cm^{-3} g^{-2}, 5 Hz
Ref. [31] (EM + TE)	3.5–7 Hz, 1g	3.67 mW cm^{-3} g^{-2}, 5 Hz
Ref. [32] (PE + EM + TE)	10–31.5 Hz, 0.5 g	2.16×10^{-2} mW cm^{-3} g^{-2}
Ref. [33] (PE + EM + TE)	2–5 Hz, 1 g	3.2 mW cm^{-3}, 5 Hz
Ref. [45] (EM + TE)	4–9 Hz, 1 g	3.15 mW cm^{-3} g^{-2}, 6 Hz
Present Work (PE + EM + TE)	1–11 Hz, 1 g	3.69 mW cm^{-3} g^{-2}, 3 Hz

*PE = Piezoelectric, EM = Electromagnetic, TE = Triboelectric.

4. Conclusions

In this work, a novel miniaturized piezoelectric-electromagnetic-triboelectric energy harvester was designed and investigated. A multi-stability based FUC approach implemented by the highly compact combination of two new configurations of magneto-multi-stable oscillators was proposed to significantly improve the dynamic performance of the harvester under ultra-low-frequency and broadband vibration sources. Through a highly compact design of various PEG, EMG and TENG units into a single multi-stable mechanical system, a significant improvement can be achieved for the power generation capability under the same mechanical motions. Theoretical models were also constructed to study the dynamic and electrical characteristics of the present harvester in both tri-stable and quad-stable modes. The fabricated prototype of the tri-hybrid harvester working in both tri-stable (vertical) and quad-stable (horizontal) states was examined under both electrodynamic shaker and human-body-induced vibration tests. The major findings of this work are summarized as follows:

- In the electrodynamic shaker test, both dynamical modes can offer a high-efficiency operating bandwidth that can cover the frequency range of 1–11 Hz under 1 g acceleration. Under a low-intensity excitation, a tri-stable mode can be more easily to be triggered into large-amplitude inter-well motions for generating high energy output. When an external excitation level is sufficiently high to activate a quad-stable mode, it shows superior performance over the tri-stable state.
- Under a 3 Hz excitation with an acceleration of 1 g, the PEG, EMG, TENG-F and TENG-CS units can generate the maximum output power of 35.37 mW, 35.08 mW, 27.12 μW and 60.99 μW across an optimum load resistance of 35 kΩ, 210 Ω, 19 MΩ and 17 MΩ, respectively. The whole prototype can reach the maximum output power of 85.65 mW, corresponding to the normalized power density of 3.69 mW cm^{-3} g^{-2} at such excitation conditions.
- Among all units, the PEG unit has the highest normalized power density, whether it is calculated either on the volume ratio (7.65 mW cm^{-3}) or the weight ratio (2.43 mW g^{-1}). While the EMG ranks second with the normalized power density of 4.62 mW cm^{-3} (volume ratio) and 1.63 mW g^{-1} (weight ratio). Owing to the highly efficient PEGs, the proposed energy harvester is flexible for miniaturization to compare with the mainstream vibration-based energy harvesting techniques that mainly reply on the function of EMG units.
- Under the test of human motions, the present energy harvester was deployed in both horizontal and vertical positions for various body positions (i.e., arm, wrist, knee and ankle). A 560 μF storage capacitor was effectively charged up to certain voltage levels due to the acceleration levels of walking and slow running. In addition, the present harvester can also power up 20 thermohygrometers and 296 LEDs continuously under various random levels of handshaking motions.

This vibration-based energy harvesting technique shows a remarkable working performance in terms of bandwidth and power density. Unleashing the potential of the present design will offer many opportunities for direct integration into various engineering fields, e.g., railway vibrations, traffic vehicles, bridge motions and construction safety monitoring (for human activities).

Acknowledgements

The work described in this paper was supported by the National Natural Science Foundation of China (Grant Nos. 12002300, 12072233 and 1872044) and the Research Impact Fund (Project No. R5020-18) and Early Career Scheme (Project No. PolyU 252026/16E) from the Research Grants Council of the Hong Kong Special Administrative Region. The funding support from the Innovation and Technology Commission of the Hong Kong Special Administrative Region to the Hong Kong Branch of National Rail Transit Electrification and Automation Engineering Technology Research Center (K-BBY1) is also gratefully acknowledged. In addition, the authors would also like to express our sincere gratitude and appreciation to the support of the Center of Sports Training and Rehabilitation, Department of Rehabilitation Sciences of The Hong Kong Polytechnic University.

References

[1] Hu YF, Yang J, Niu SM, Wu WZ, Wang ZL. Hybridizing Triboelectrification and Electromagnetic Induction Effects for High-Efficient Mechanical Energy Harvesting. ACS Nano 2014; 8: 7442-7450.

[2] Aldawood G, Nguyen HT, Bardaweel H. High power density spring-assisted nonlinear electromagnetic vibration energy harvester for low base-accelerations. Applied Energy 2019; 253: 113546.

[3] Chen C, Sharafi A, Sun JQ. A high density piezoelectric energy harvesting device from highway traffic - Design analysis and laboratory validation. Applied Energy 2020; 269:15073.

[4] Erturk A, Inman DJ. Piezoelectric Energy Harvesting. Wiley, Chichester, UK, 2011.

[5] Gu YH, Liu WQ, Zhao CY, Wang P. A goblet-like non-linear electromagnetic generator for planar multi-directional vibration energy harvesting. Applied Energy 2020; 266: 114846.

[6] Parida K, Kumar V, Jiangxin W, Bhavanasi V, Bendi R, Lee PS, Highly Transparent, Stretchable, and Self-Healing Ionic-Skin Triboelectric Nanogenerators for Energy Harvesting and Touch Applications, Advanced Materials 2017; 29: 1702181.

[7] Yang X, Wang C, Lai SK. A magnetic levitation-based tristable hybrid energy harvester for scavenging energy from low-frequency structural vibration. Engineering Structures 2020; 221: 110789.

[8] Salauddin Md, Toyabur RM, Maharjan P, Park JY. High performance human-induced vibration driven hybrid energy harvester for powering portable electronics. Nano Energy 2018; 45: 236-246.

[9] Chen LH, Xue JT, Pan SQ, Chang LQ. Study on cantilever piezoelectric energy harvester with tunable function. Smart Materials and Structures 2020; 29: 075001.

[10] Song H, Kumar P, Sriramdas R, Lee H, Sharpes N, Kang M, et al. Broadband dual phase energy harvester: Vibration and magnetic field. Applied Energy 2018; 225:1132-1142.

[11] Daqaq MF, Masana R, Erturk A, Quinn DD. On the Role of nonlinearities in vibratory energy harvesting: a critical review and discussion. Applied Mechanics 2014; 66: 040801.

[12] Roundy S, Zhang Y. Toward self-tuning adaptive vibration-based microgenerators. Smart Materials, Nano- and Micro-Smart Systems 2015, Sydney, Australia.

[13] Kumar A, Ali SF, Arockiarajan A. Exploring the benefits of an asymmetric monostable potential

function in broadband vibration energy harvesting. Applied Physics Letters 2018; 112: 233901.

[14] Zhou SX, Cao JY, Inman DJ, Lin J, Liu SS, Wang ZZ. Broadband tristable energy harvester: Modeling and experiment verification. Applied Energy 2014; 133: 33-39.

[15] Wang C, Zhang QC, Wang W, Feng JJ. A low-frequency, wideband quad-stable energy harvester using combined nonlinearity and frequency up-conversion by cantilever-surface contact. Mechanical Systems and Signal Processing 2018; 112: 305-318.

[16] Wang C, Zhang QC, Wang W. Low-frequency wideband vibration energy harvesting by using frequency up-conversion and quin-stable nonlinearity. Journal of Sound and Vibration 2017; 399: 169-181.

[17] Wang C, Lai SK, Wang ZC, Wang JM, Yang WQ, Ni YQ. A low-frequency, broadband and tri-hybrid energy harvester with septuple-stable nonlinearity-enhanced mechanical frequency up-conversion mechanism for powering portable electronics. Nano Energy 2019; 64: 103943.

[18] Lai SK, Wang C, Zhang LH, A nonlinear multi-stable piezomagnetoelastic harvester array for low-intensity, low-frequency, and broadband vibrations. Mechanical Systems and Signal Processing 2019; 122: 87-102.

[19] Lallart M, Zhou SX, Yang ZC, Yan LJ, Li K, Chen Y. Coupling mechanical and electrical nonlinearities: The effect of synchronized discharging on tristable energy harvesters. Applied Energy 2020; 266: 114516.

[20] Gu L, Livermore C. Impact-driven, frequency up-converting coupled vibration energy harvesting device for low frequency operation. Smart Materials and Structures 2011; 20: 045004.

[21] Kathpalia B, Tan D, Stern I, Erturk A. An experimentally validated model for geometrically nonlinear plucking-based frequency-up conversion in energy harvesting. Smart Materials and Structures 2018; 27:15024.

[22] Tang L, Yang Y, Soh CK. Improving functionality of vibration energy harvesters using magnets. Journal of Intelligent Material Systems and Structures 2012; 23:1433-49.

[23] Han D, Yun KS. Piezoelectric energy harvester using mechanical frequency up conversion for operation at low-level accelerations and low-frequency vibration. Microsystem Technologies 2015; 21(8):1669-76.

[24] Wu Y, Ji H, Qiu J, Liu W, Zhao J. An internal resonance based frequency up-converting energy harvester. Journal of Intelligent Material Systems and Structures 2018;29(13):2766-81.

[25] Quan T, Wu YC, Yang Y. Hybrid electromagnetic-triboelectric nanogenerator for harvesting vibration energy. Nano Research 2015; 8: 3272.

[26] Fan KQ, Liu SH, Liu HY, Zhu YM, Wang WD, Zhang DX. Scavenging energy from ultra-low frequency mechanical excitations through a bi-directional hybrid energy harvester. Applied Energy 2018; 216: 8-20.

[27] Saadatnia Z, Esmailzadeh E, Naguib HE. Design, simulation, and experimental characterization of a heaving triboelectric-electromagnetic wave energy harvester. Nano Energy 2018; 50: 281-290.

[28] Salauddin Md, Toyabur RM, Maharjan P, Rasel MS, Kim JW, Cho H, et al. High performance human-induced vibration driven hybrid energy harvester for powering portable electronics. Nano Energy 2018; 45: 236-246.

[29] Li ZJ, Li T, Yang ZB, Naguib HE. Toward a 0.33W piezoelectric and electromagnetic hybrid energy harvester: Design, experimental studies and self-powered applications. Applied Energy 2019; 255: 113805.

[30] Dong K, Peng X, Wang ZL. Fiber/Fabric-Based Piezoelectric and Triboelectric Nanogenerators for Flexible/Stretchable and Wearable Electronics and Artificial Intelligence. Advanced Materials 2020; 32: 1902549.

[31] Toyabur RM, Sohel Rana SM, Salauddin Md, Maharjan P, Bhatta T, Kim H, et al. A highly miniaturized freestanding kinetic-impact-based non-resonant hybridized electromagnetic-triboelectric nanogenerator for human induced vibrations harvesting. Applied Energy 2020; 279: 115799.

[32] He J, Wen T, Qian S, Zhang ZX, Tian ZM, Zhu J, et al. Triboelectric-piezoelectric-electromagnetic hybrid nanogenerator for high-efficient vibration energy harvesting and self-powered wireless monitoring system. Nano Energy 2018; 43: 326-339.

[33] Tan PC, Zheng Q, Zou Y, Shi BJ, Jiang DJ, Qu XC, et al. A battery-like self-charge universal module for motional energy harvest. Advanced Energy Materials 2019; 9: 1901875.

[34] Rodrigues C. Gomes A, Ghosh A, Pereira A, Ventura J. Power-generating footwear based on a triboelectric-electromagnetic-piezoelectric hybrid nanogenerator. Nano Energy 2019; 62: 660-666.

[35] Cai M, Yang Z, Cao J, Liao WH. Recent advances in human motion excited energy harvesting

systems for wearables, Energy Technology, 2020; 8: 2000533.

[36] Chen C, Chau LY, Liao WH. A knee-mounted biomechanical energy harvester with enhanced efficiency and safety, Smart Materials and Structures, 2017; 26: 065027.

[37] Zhou SX, Zuo L. Nonlinear dynamic analysis of asymmetric tristable energy harvesters for enhanced energy harvesting. Communications in Nonlinear Science and Numerical Simulation 2018; 61: 271-284.

[38] Niu S, Wang ZL, Theoretical systems of triboelectric nanogenerators, Nano Energy 2014; 14: 161-192.

[39] Niu S, Liu Y, Chen XY, Wang SH, Zhou YS, Lin L, et al. Theory of freestanding triboelectric-layer-based nanogenerators. Nano Energy 2015; 12: 760-774.

[40] Panyam M, Daqaq MF. Characterizing the effective bandwidth of tri-stable energy harvesters. Journal of Sound and Vibration 2017; 386: 336-358.

[41] Wei X Y, Zhu G, Wang ZL. Surface-charge engineering for high performance triboelectric nanogenerator based on identical electrification materials. Nano Energy 2014; 10: 83–89.

[42] Wang SH, Zi YL, Zhou YS, Li SM, Fan FR, et al. Molecular surface functionalization to enhance the power output of triboelectric nanogenerators. Journal of Materials Chemistry A 2016; 4: 3728–3734.

[43] Tang W, Jiang T, Fan FR, Yu AF, Zhang C, et al. Liquid-metal electrode for high-performance triboelectric nanogenerator at an instantaneous energy conversion efficiency of 70.6%. Advanced Functional Materials 2015; 25: 3718–3725.

[44] Bo LD, Turco PGE. Analysis and scaling study of vibration energy harvesting with reactive electromagnetic and piezoelectric transducers. Journal of Sound and Vibration 2020; 484: 115510.

[45] Rahman MT, Rana SS, Salauddin M, Maharjan P, Bhatta T, Park JY. Biomechanical Energy-Driven Hybridized Generator as a Universal Portable Power Source for Smart/Wearable Electronics. Advanced Energy Materials 2020; 10: 1903663.